J. Chem. Sci. Vol. 129, No. 3, March 2017, pp. 381–395.
DOI 10.1007/s12039-017-1230-5

REGULAR ARTICLE

Sol-gel-*cum*-hydrothermal synthesis of mesoporous Co-Fe@Al_2O_3−MCM-41 for methylene blue remediation

AMARESH C PRADHAN*, ANIMESH PAUL and G RANGA RAO*

Department of Chemistry, Indian Institute of Technology Madras, Chennai, Tamil Nadu 600 036, India
Email: amaresh32@gmail.com; grrao@iitm.ac.in

MS received 15 October 2016; revised 28 December 2016; accepted 3 January 2017

Abstract. A combined sol-gel-*cum*-hydrothermal method has been employed to synthesize novel monometallic (Mn, Fe, Co) and bimetallic (Co-Fe, Mn-Co, Fe-Mn) nanoparticles loaded onto Al_2O_3−MCM-41. Powder XRD, N_2 sorption, field emission scanning electron microscopy (FESEM) and high resolution transmission electron microscopy (HRTEM) measurements show that the materials possess mesoporosity, high surface area and nanosize. Monometallic Fe, Co and Mn @Al_2O_3−MCM-41 and bimetallic Co-Fe, Fe-Mn and Mn-Co @Al_2O_3−MCM-41 materials were tested for methylene blue remediation from aqueous media. In the present study, Co-Fe@Al_2O_3−MCM-41 was found to be an excellent adsorbent. The adsorption efficiency of Co-Fe@Al_2O_3−MCM-41 has been studied as a function of adsorbent dose and pH of the solution. Maximum adsorption of methylene blue was obtained at high pH values of the solution. Framework mesoporosity, high surface area, and narrow pore distribution are the key factors for an efficient adsorption of methylene blue on Co-Fe@Al_2O_3−MCM-41.

Keywords. Oxides; sol-gel; adsorption; surface properties; composite materials.

1. Introduction

Industrial dyes and dye related compounds show adverse effects on the aquatic life and the ecosystem.[1–4] In general, dyes are categorized as cationic dyes (methylene blue, rhodamine B and 6G, methyl violate, methylene green, Malachite green, cationic red X-GRL), anionic dyes (methyl orange, eosin Y, methyl red, acid green 25, Congo red, N719), phenolic compounds (bromophenol blue, bisphenol A, phenol, 2-chloro-4-nitrophenol, 4-chloro-2-nitrophenol) and other dye molecules such as para red (azo dye), alizarin (mordant dye) and indanthrene blue (vat dye). Some of these dye molecules are considered as contaminants and their remediation is studied extensively by adsorption on porous materials,[5–12] photocatalytic degradation using semiconducting oxide materials,[13–17] photo-Fenton oxidation by Fe-based materials,[18–21] biological degradation[22] and degradation by graphene-based materials.[23–27] Among these methods, adsorption process is cost-effective and reproducible for the removal of pollutant molecules.[2,18] The major advantage of the adsorption process is that it does not require any chemicals and UV radiation, and hence widely accepted in water purification industry.

Porous materials such as MCM-41 with high textural properties such as surface area, narrow pore diameter and large pore volume are preferred for efficient adsorption and removal of pollutant molecules.[28,29] For example, MCM-41 framework with surface area greater than 1000 m^2 g^{-1} and pore diameter of about 2–3 nm can effectively be used to trap methylene blue molecules of molecular volume 0.4 nm × 0.61 nm × 1.43 nm.[30] Moreover, loading of aluminum into the framework of MCM-41 leads to isomorphous substitution of aluminum for silicon which creates ion exchange sites in the molecular sieve framework.[31] This ion exchange property within the Al_2O_3−MCM-41 may aid the adsorption of methylene blue on the material. In transition metal oxides, vanadium doped TiO_2 and magnetite show remarkable enhancement of the adsorption capacity by an order of magnitude compared to pure oxides, which significantly promotes the adsorption and degradation of methylene blue.[32] Further, hydrogen bonding between the associated hydroxyl groups on the adsorbent surface with the lone electron pair on nitrogen and sulphur atoms of aromatic rings in methylene blue structure can also play a significant role in the adsorption of methylene blue.[33] Monometallic and bimetallic particles are embedded in porous frameworks associated with Al_2O_3–MCM-41 which are expected to show good dye adsorption properties.[20,21] This is possible because, (i) the pore

*For correspondence

diameter (2–3 nm) in the framework of monometallic and the bimetallic@Al_2O_3−MCM-41 is compatible with molecular diameter of methylene blue, (ii) framework mesoporosity, and (iii) high surface area of mono and bimetallic@Al_2O_3-MCM-41.

In the present study, we have explored monometallic Fe, Co and Mn@Al_2O_3−MCM-41, and bimetallic Co-Fe, Fe-Mn and Mn-Co@Al_2O_3−MCM-41 as stable and active adsorbents for the removal of methylene blue from aqueous solutions. We have loaded monometallic (Mn, Fe, Co) and bimetallic (Co-Fe, Fe-Mn, Mn-Co) particles into tailor-made *in situ* mesoporous Al_2O_3−MCM-41. The dye adsorption was found to be highly efficient on Co-Fe@Al_2O_3−MCM-41 under basic conditions.

2. Experimental

2.1 *Preparation of mesoporous Al_2O_3*

Mesoporous Al_2O_3 was synthesized by sol-gel method. Cetyltrimethylammonium bromide (CTAB, $C_{19}H_{42}NBr$, Aldrich, 99%) was used as structure directing agent and aluminium isopropoxide (99%, Sigma-Aldrich) as alumina source. Initially, CTAB was dissolved in water in order to form micelles. Then, aluminium isopropoxide was added and stirred for 2 h. The molar ratio of CTAB and aluminium isopropoxide was kept at 1:1. Ammonia was added to maintain the pH of the solution at 10 and the suspension was stirred for 12 h. Final product was filtered, washed with distilled water and ethanol before drying them at 70°C for 12 h. The mesoporous Al_2O_3 powder was obtained by calcining the material at 600°C for 6 h.

2.2 *Synthesis of MCM-41*

MCM-41 was prepared by sol-gel-*cum*-hydrothermal method. 2.4 g of CTAB was added to 120 mL water and then, 8 mL of aqueous NH_3 was added into it. Stoichiometric amount of tetraethyl orthosilicate (TEOS, $C_8H_{20}O_4$ Si, Aldrich, 99%) was added to the solution under vigorous stirring for 1 h. The gel was transferred into stainless steel autoclave and placed in a furnace for 20 h at 120°C. The final product was filtered and dried at 70°C for 12 h. The surfactant was removed from the product by calcining at 550°C in air for 5 h.

2.3 *Fabrication of monometallic and bimetallic@Al_2O_3−MCM-41*

In a typical synthesis, 2.5 g of CTAB was added to 120 mL of H_2O and stirred for one hour and then 0.377 g of mesoporous Al_2O_3 was added to it. The mixture was continuously stirred by adding 10 mL aqueous NH_3 after an hour. Then, 8 mL of TEOS silica source was added to the mixture and stirred for 2 h (solution A) to obtain Al_2O_3−MCM-41 with Si/Al ratio 10. Then 1.0 mmol of $FeSO_4.7H_2O$ was dissolved in 20 mL ethanol and 5 mL of oleic acid was added and stirred for two hours (solution B). Solutions A and B were mixed and stirred for 2 h. The total mixture was transferred into a stainless steel autoclave and put into a furnace for 20 h at 120°C. The gel was washed with distilled water and ethanol, and further dried in an oven at 70°C for 12 h. The white powder was calcined at 500°C at 5 h in air. This material is denoted as Fe@Al_2O_3−MCM-41. Similar procedure was adopted to synthesize Co@Al_2O_3−MCM-41 and Mn@Al_2O_3−MCM-41 samples by taking 1.0 mmol cobalt(II) nitrate hexahydrate ($Co(NO_3)_2.6H_2O$) and 1.0 mmol of manganous acetate tetrahydrate ($C_4H_6MnO_4.4H_2O$), respectively. The experimental weight of monometallic Fe, Co and Mn is 0.056 g, 0.058 g and 0.055 g in 1 g of Fe@Al_2O_3−MCM-41, Co@Al_2O_3−MCM-41 and Mn@Al_2O_3−MCM-41, respectively.

For synthesis of bimetallic@Al_2O_3−MCM-41, 0.5 mmol of $Co(NO_3)_2.6H_2O$ and 0.5 mmol of $FeSO_4.7H_2O$ are mixed in ethanol. The above synthesis procedure was followed to obtain Co-Fe@Al_2O_3−MCM-41, Fe-Mn@Al_2O_3−MCM-41 and Mn-Co@Al_2O_3−MCM-41 samples. The experimental weight of bimetallic Co and Fe is 0.029 g and 0.028 g in 1 g of Co-Fe@Al_2O_3−MCM-41 sample. Similar calculated weight ratio of the two metals was maintained in both Fe-Mn@Al_2O_3−MCM-41 and Mn-Co@Al_2O_3−MCM-41.

2.4 *Characterization of materials*

The X-ray diffraction patterns (XRD) of the materials were obtained by employing Bruker AXS D8 Advance diffractometer and Cu Kα ($\lambda = 0.15408$ nm) radiation. A scan rate of 2°/min was used to record high angle reflections from 10 to 8°, and 0.01°/s scan rate for low angle reflections from 0.5 to 10°. The specific surface area, pore size and pore volume were measured by N_2 adsorption-desorption method at liquid nitrogen temperature (−196°C) using Micromeritics ASAP 2020. The specific surface area and pore size distribution were estimated based on Brunauer-Emmett-Teller (BET) and Barrett-Joyner-Halenda (BJH) methods, respectively. For the field emission scanning electron microscopy (FESEM) analysis, powder samples were dispersed on a conducting carbon tape by FEI Quanta 400 instrument. Transmission electron microscopy (TEM) images were obtained using Philips CM 200 transmission electron microscope with a LaB_6 filament and equipped with an ultrathin objective lens and CCD camera. HRTEM images were recorded by using JEOL 3010 machine. Diffuse reflectance UV-Vis (DRUV-Vis) spectra of the materials were performed by JASCO V-660 spectrophotometer equipped with 60 mm integrating sphere. The measurements were carried out at a bandwidth of 5 nm in the wavelength range of 200–800 nm at a scanning speed of 100 nm/min. The FTIR spectra of the samples were recorded with JASCO FTIR-4100 spectrophotometer in the range of 400–4000 cm^{-1} at room temperature using KBr as reference. The zeta potential of the material was measured by equilibrating 5 mg of Co-Fe@Al_2O_3−MCM-41 adsorbent powder

in 50 mL of 0.01 M KCl solution using Zetasizer Nano ZS (Malvern, UK).

2.5 *Adsorption procedure*

Methylene blue was obtained from Merck, India. A 100 mg/L stock solution of methylene blue was prepared and suitably diluted to the required initial concentration. Adsorption studies were carried out by taking 20 mL of 100 mg/L methylene blue solution and 0.02 g of adsorbent dose at pH = 10. The solution was taken in a tightly fitted conical flask and the pH of the solution was adjusted by adding 0.01 M HNO_3 and/or ammonia (Merck GR grade). Systronics μ pH system 361 was employed to monitor the pH while stirring. The adsorption process was completed in 3 h. The solution was centrifuged and analysed by JASCO V-660 UV-visible spectrophotometer. The maximum absorbance of methylene blue occurs at 664 nm. The percentage of methylene blue remaining in the solution was calculated by $\frac{C}{C_0} \times 100\%$, where C and C are the initial concentration and concentration of methylene blue after adsorption, respectively.

3. Results and Discussion

3.1 *XRD analysis*

Figure 1 shows the XRD pattern of mesoporous Al_2O_3 and monometallic and bimetallic@Al_2O_3−MCM-41 samples. Mesoporous Al_2O_3 is crystalline in nature showing diffraction peaks at (440), (400) and (311) due to γ-phase.[34] However, the diffraction peaks of γ-Al_2O_3 phase are very feeble in monometallic and bimetallic@Al_2O_3−MCM-41 systems. The metal loaded Al_2O_3−MCM-41samples are substantially amorphous in nature and do not show any x-ray reflections of the respective metal oxide phases. The broad band centred at $2\theta = 22^\circ$ can be assigned to the characteristic refection from amorphous SiO_2 (JCPDS29-0085). The XRD results indicate that Al_2O_3−MCM-41 matrix is highly amorphous in which cluster-like Fe, Co, Mn, Co-Fe, Mn-Co, Fe-Mn oxide species are embedded.

The representative low angle XRD pattern for MCM-41, Al_2O_3−MCM-41 and Co-Fe@Al_2O_3−MCM-41 samples are shown in Figure 2. The three samples exhibited highly intense d_{100} diffraction peak at low angle indicating the mesoporous nature.[35] It was observed that the peak intensity (d_{100}) slightly decreased from MCM-4 to Al_2O_3−MCM-41 and extensively decreased from Al_2O_3−MCM-41 to Co-Fe@Al_2O_3−MCM-41. This is due to the loading of the mesoporous Al_2O_3 into the extra-framework of the MCM-41 and loading of the (Co and Fe) onto the surface of the Al_2O_3−MCM-41.[21] The other three reflections indexed as d_{110}, d_{200} and d_{210} were comparatively less intense. This suggests the presence of a periodic hexagonal arrangement of the channel.[36] The MCM-41 shows d_{100}, d_{110}, d_{200} and d_{210} reflections, indicating well-ordered hexagonal mesoporous channel. The (100) and (110) diffraction peaks related to Al_2O_3−MCM-41 are intact, indicating that addition of mesoporous Al_2O_3 powder into the MCM-41 does not affect the mesoporosity and periodic hexagonal arrangement of the channel. This phenomenon is due to, (i) the isomorphous of substitution of Si^{4+} by Al^{3+}

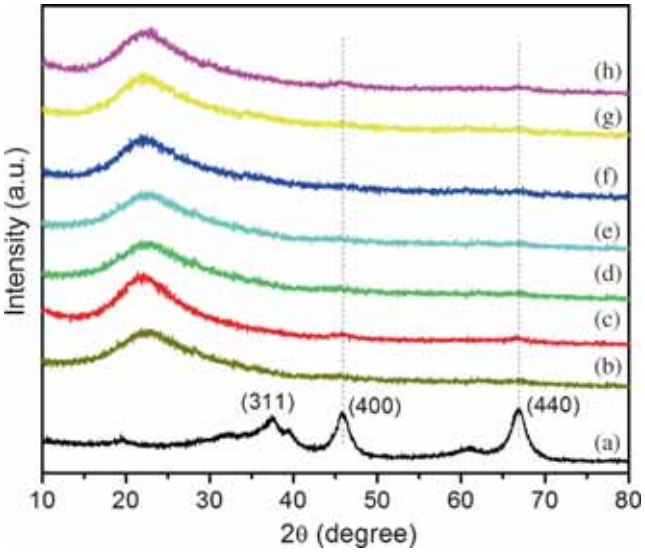

Figure 1. High angle x-ray diffractorgrams of (a) Al_2O_3, (b) MCM-41, (c) Co@Al_2O_3−MCM-41, (d) Mn@Al_2O_3−MCM-41, (e) Fe@Al_2O_3−MCM-41, (f) Mn-Co@Al_2O_3−MCM-41, (g) Fe-Mn@Al_2O_3−MCM-41, and (h) Co-Fe@Al_2O_3−MCM-41 materials.

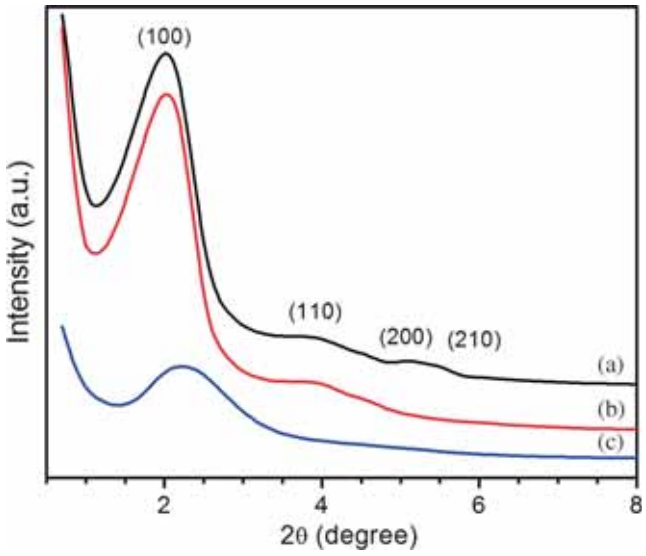

Figure 2. Low angle x-ray diffractorgrams of (a) MCM-41, (b) Al_2O_3−MCM-41 and (C) Co-Fe@Al_2O_3−MCM-41 materials.

in MCM-41 without affecting its mesoporosity and periodicity,[37] and (ii) the coordination of Al^{3+} ions with Si^{4+} through oxygen leading to extra-framework modification of MCM-41.[21] Loading of Fe and Co onto the mesoporous Al_2O_3−MCM-41 leads to the degeneration of structural order as shown by weak d_{100} plane and disappearance of reflections (110), (200) and (210) in Figure 2c. This is because some Co and Fe particles tend to block the pores of Al_2O_3−MCM-41 network. Similar behaviour can be predicted in all monometallic and bimetallic@Al_2O_3−MCM-41 materials.

3.2 *N_2 sorption studies*

The N_2 sorption isotherms of the materials are shown in Figures 3 and 4. All the materials showed type-IV isotherm with H1 hysteresis. This isotherm represents the mesoporous behaviour of the material.[38] The adsorption step of MCM-41, Al_2O_3−MCM-41 material (Figure 3) centred in the relative pressure (P/P_0) region from 0.1 to 0.5. This phenomenon indicates the presence of framework-confined mesopores or framework mesoporosity/intra-particle mesoporosity.[39,40] The nature of sorption step in MCM-41 as well as Al_2O_3−MCM-41 is tall and sharp which indicates the framework mesoporosity. The adsorption step of mesoporous Al_2O_3 meet with desorption curve at relative pressure (P/P_0) in the region of 0.5. This can be treated as a border line framework mesoposity. The sorption isotherms of monometallic (Fe, Co, Mn) and bimetallic (Co-Fe, Fe-Mn, Mn-Co) @Al_2O_3−MCM-41 systems are presented in Figure 4. The hysteresis loops for monometallic and bimetallic@Al_2O_3−MCM-41 samples begin at a relative pressure of about 0.45, which indicates the framework mesoporosity.

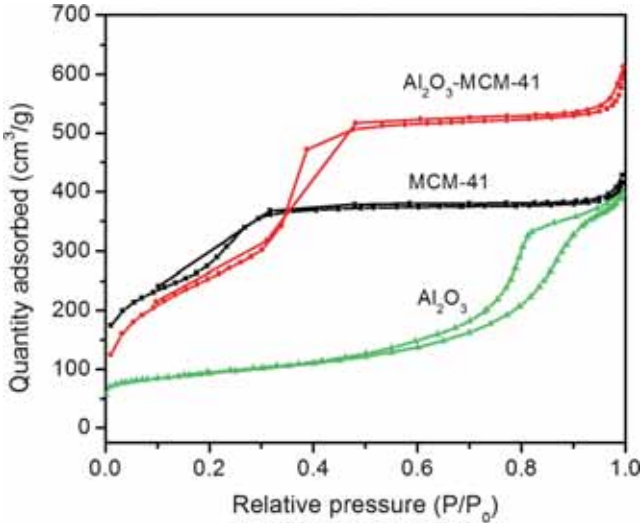

Figure 3. N_2 sorption isotherms of Al_2O_3, MCM-41 and Al_2O_3−MCM-41 materials.

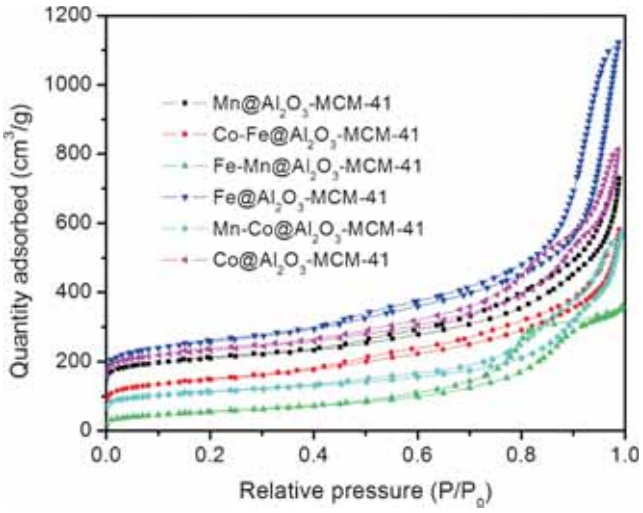

Figure 4. N_2 sorption isotherms of Mn@Al_2O_3−MCM-41, Co-Fe@Al_2O_3−MCM-41, Fe-Mn@Al_2O_3−MCM-41, Fe@Al_2O_3−MCM-41, Mn-Co@Al_2O_3−MCM-41and Co@Al_2O_3−MCM-41 materials.

The pore size distribution curves are shown in Figure 5. The result shows that mono modal and narrow mesoporous range between 2–3 nm, except mesoporous Al_2O_3 of 3.6 nm. This indicates the presence of framework mesoporosity in MCM-41 and Al_2O_3−MCM-41, whereas Al_2O_3 is attributed to the border line framework mesoporosity. This is because the pore diameter of Al_2O_3 is nearer to narrow range (2–3 nm). Figure 6 represents the pore size distribution curves of mono and bimetallic@Al_2O_3−MCM-41 materials. These materials are also in similar framework mesoporosity as that of MCM-41 and Al_2O_3−MCM-41 materials.

The surface area, pore diameter, pore volume of samples are summarized in Table 1. These values are

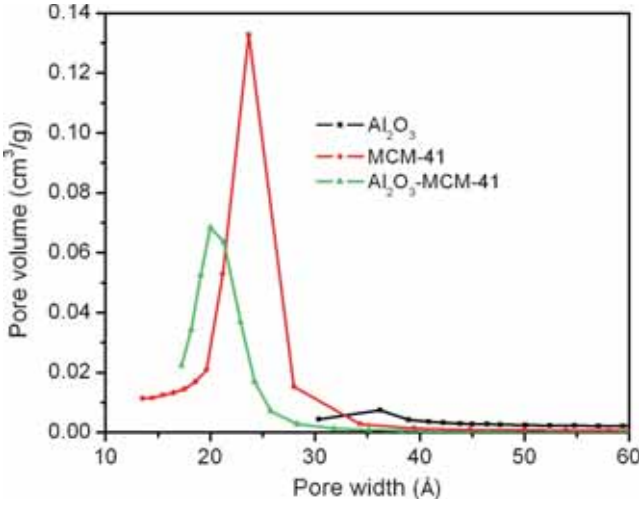

Figure 5. Pore size distributions of Al_2O_3, MCM-41 and Al_2O_3−MCM-41 materials.

obtained from N_2 sorption isotherms. The high specific surface area of Al_2O_3−MCM-41as compared to MCM-41 indicates that the meso-Al_2O_3 is incorporated into the extra-framework of the MCM-41. In other words, the high texture mesoporous Al_2O_3 has been incorporated into the extra-framework of MCM-41 by coordination of Al^{3+} to Si^{4+}.[21] The other factor is mesoporous Al_2O_3 hinders the crystal growth of MCM-41 which aids to increase the surface area of Al_2O_3−MCM-41. After loading of monometallic system such as Fe, Co and Mn onto the surface of mesoporous Al_2O_3−MCM-41, the surface area decreases as compared to pure Al_2O_3−MCM-41. This is because blocking of the mesopore network by the metal. Bimetallic systems, Co-Fe, Fe-Mn and Mn-Co incorporated Al_2O_3−MCM-41 materials show much less surface area as compared to monometallic@Al_2O_3−MCM-41. The pore blocking is more effective in the case of bimetallic materials compared to monometallic materials.

3.3 *FTIR spectral analysis*

The FTIR spectra of MCM-41 and mesoporous Al_2O_3−MCM-41 are shown in the Figure 7. The anti-symmetric Si−O−Si vibration bands of MCM-41 and Al_2O_3−MCM-41 samples are at 1089 and 1082 cm^{-1}, respectively.[41] This shift is attributed to the incorporation of Al_2O_3 into SiO_2 matrix in MCM-41. The increase in the mean Si−O distances in the walls is caused by the substitution of small size Si^{4+} ($r_{Si^{4+}} = 40$ pm) by the large aluminium ion ($r_{Al^{3+}} = 53.5$ pm).[42] The absorption band at 967 cm^{-1} (MCM-41) decreases to 961 cm^{-1} (Al_2O_3−MCM-41), which is assigned to the stretching vibration of unsubstituted −Si−O−Si− and Al_2O_3-

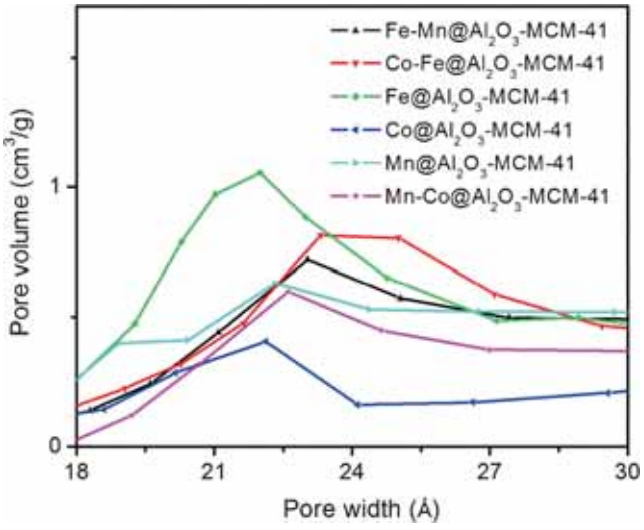

Figure 6. Pore size distributions of Fe-Mn@Al_2O_3−MCM-41, Co-Fe@Al_2O_3−MCM-41 Fe@Al_2O_3−MCM-41, Co@Al_2O_3−MCM-41, Mn@Al_2O_3−MCM-41 and Mn-Co@Al_2O_3−MCM-41 materials.

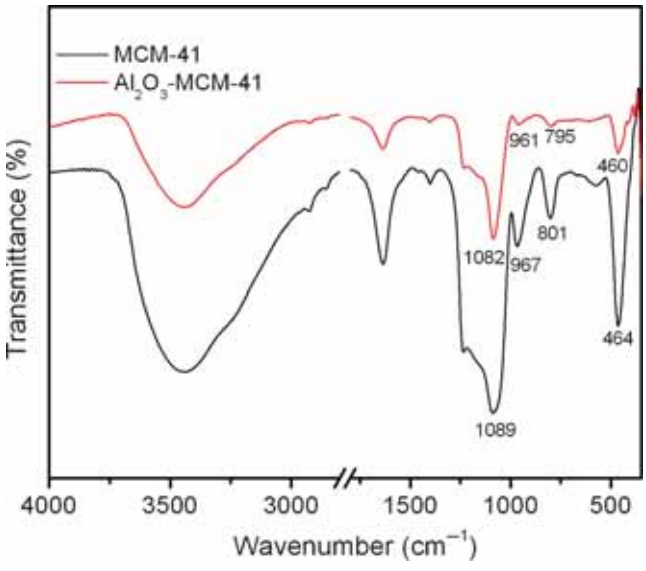

Figure 7. FTIR spectra of MCM-41 and Al_2O_3−MCM-41 samples.

Table 1. Textural properties of Al_2O_3, MCM-41, Al_2O_3−MCM-41, monometallic @Al_2O_3−MCM-41 and bimetallic@Al_2O_3−MCM-41 materials measured by BET method.

Samples	Surface area (m^2/g)	Pore volume (cm^3/g)	Pore diameter (nm)
Al_2O_3	268	0.67	3.6
MCM-41	800	1.10	2.2
Al_2O_3−MCM-41	870	1.78	2.1
Fe@Al_2O_3−MCM-41	379	0.96	2.2
Co@Al_2O_3−MCM-41	321	0.95	2.2
Mn@Al_2O_3−MCM-41	308	0.94	2.2
Co-Fe@Al_2O_3−MCM-41	300	0.93	2.3
Mn-Co@Al_2O_3−MCM-41	275	0.85	2.3
Fe-Mn@Al_2O_3−MCM-41	265	0.79	2.3

incorporated −Si−O−Si− (−Si−O−Al−), respectively. This is generally considered as a proof for the incorporation of heteroatom into MCM-41.[41] The absorption bands at 1057 and 1225 cm^{-1} are typically from the asymmetric stretching vibrations of Si–O–Si bridges, for both MCM-41 and Al_2O_3−MCM-41.[43] When Al_2O_3 is incorporated in MCM-41, small shifts are observed in the vibrational bands from 801 to 795 cm^{-1} and 464 to 460 cm^{-1} (Figure 7). These shifts provide evidence for the incorporation of Al_2O_3 into MCM-41.[40]

The FTIR spectra of mono and bimetallic@Al_2O_3−MCM-41 are presented in the Figure 8. The band at 1640 cm^{-1} is attributed to the bending mode of water present in all the samples. The two broad vibrational bands at 1028 and 1232 cm^{-1} are due to asymmetric stretching vibrations of –Si–O–Si– bridges present in mono and bimetallic@Al_2O_3−MCM-41 systems.[43] Moreover, the −Si–O–Si− vibrational bands in pure MCM-41 (1089 cm^{-1}) and Al_2O_3−MCM-41 (1082 cm^{-1}) have been shifted to lower values in mono and bimetallic@Al_2O_3−MCM-41 systems. This occurs because there is an increase in mean Si–O distance in the walls caused by the loading of metallic ions of larger radius. The remnant vibrational band at 975 cm^{-1} is assigned to the stretching vibration of −Si−O−M or M−Si−M (M = Al, Fe, Co, Mn, Co-Fe, Fe-Mn and Mn-Co).[44] The Al, Fe, Co, Mn, Co-Fe, Fe-Mn and Mn-Co coordinate with Si atom through oxygen atom formed oxide composite. The weak vibrational band at 975 cm^{-1} in metal loaded systems is the same as the relatively intense vibrational band at 967 cm^{-1} in pure MCM-41 (Figure 7). The blue shift and loss of intensity of this band in Figure 8 are attributed to the loading of mono and bimetallic systems onto Al_2O_3−MCM-41 framework.[40] The bands observed at 796 cm^{-1} and 460 cm^{-1} are assigned to the symmetric stretching vibration of T−O−T unit (T= Si, Al, Fe, Co, Mn, Co-Fe, Fe-Mn and Mn-Co).[44] This is also an evidence for loading and formation of mono and bimetallic oxides within Al_2O_3−MCM-41 framework. The full FTIR spectrum of mesoporous alumina is presented in Supplementary Information (Figure S1). The peak at 1400 cm^{-1} is due to Al–OH species in the mesoporous Al_2O_3. The shoulder at 909 cm^{-1} is assigned to tetrahedral AlO_4 units while the peaks in the region 530–620 cm^{-1} are identified as octahedral AlO_6 unit.[34] These peak positions have changed due to the loading of metallic species as discussed above.

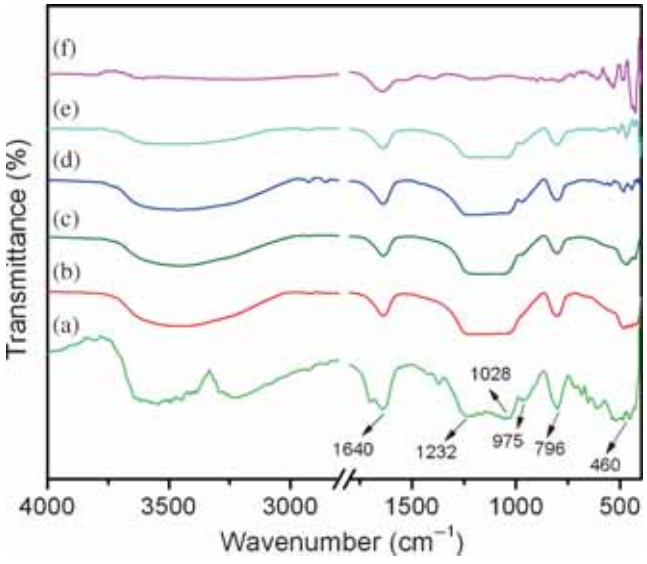

Figure 8. FTIR spectra. (a) Fe@Al_2O_3−MCM-41, (b) Co@Al_2O_3−MCM-41, (c) Mn@Al_2O_3−MCM-41, (d) Co-Fe@Al_2O_3−MCM-41, (e) Fe-Mn@Al_2O_3−MCM-41, and (f) Mn-Co@Al_2O_3−MCM-41 materials.

3.4 *Microscopy studies*

The FESEM image gives an account of surface morphology of the materials. The FESEM pictures of the Co@Al_2O_3−MCM-41, Fe@Al_2O_3−MCM-41 and Co-Fe@Al_2O_3−MCM-41 are shown in Figure 9. These micrographs reveal that the materials have spongy nature consisting of small particles and appear to be mesoporous in nature.

The energy dispersive X-ray (EDX) spectroscopy was used to characterize the surface composition of the Co-Fe@Al_2O_3−MCM-41 (Figure 10(a)). The peak intensities of elements show that the composite Co-Fe@Al_2O_3−MCM-41 contains high amount of Si and Al and less amounts of Co and Fe. Figure 10(b) demonstrates the EDX mapping analysis of Co-Fe@Al_2O_3−MCM-41. As seen from Figure 10(b), the high distribution of Si and Al elements was homogeneous and spread on the whole surface of the Co-Fe@Al_2O_3−MCM-41, indicating that the composite contains high amount of Si. The less distribution of Al as compared to Si is also detected which is consistent with the experimental procedure. In addition, the elements of Co and Fe are distributed very less as compared to Si and Al, revealing that percentage of Co and Fe are less in the composite. The amount of Co and Fe is very less but they formed respective oxides by combining with oxygen. The formation of metal oxides has been proved by the presence of O in EDX mapping. Thus, the EDX spectrum and EDX mapping depict the presence and distribution of elements in particular surface of Co-Fe@Al_2O_3−MCM-41.

The representative HRTEM micrographs of MCM-41 and Al_2O_3–MCM-41 are shown in Figure 11. The mesoporous silica exhibited highly ordered hexagonal array of pore structure of typical MCM-41, which is clearly shown in the Figures 11(a) and (b). The SAED

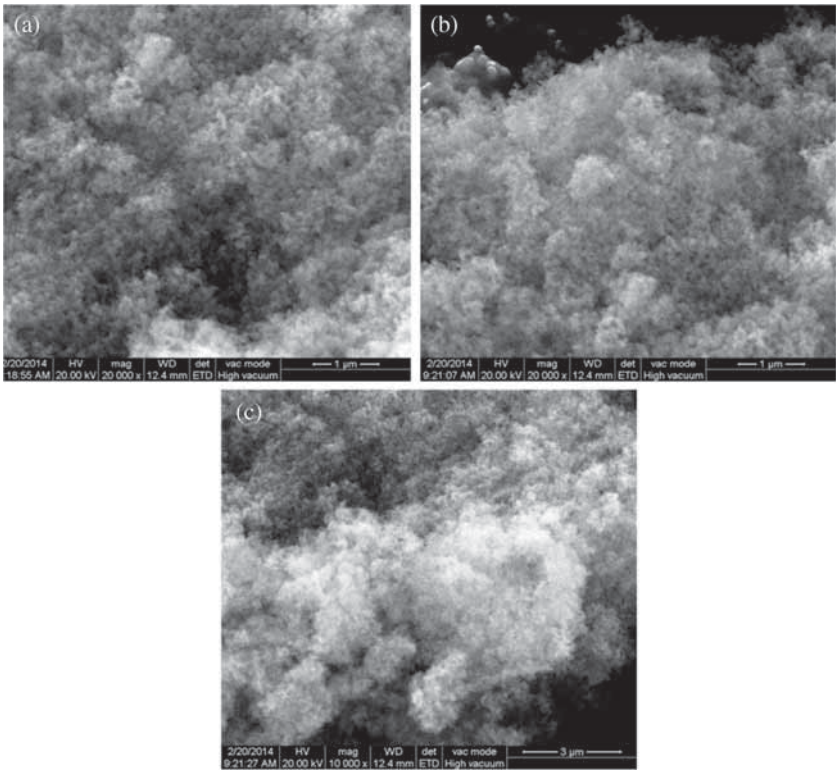

Figure 9. FESEM micrographs of (a) Co@Al_2O_3−MCM-41, (b) Fe@Al_2O_3−MCM-41 and (C) Co-Fe@Al_2O_3−MCM-41 materials.

image (Figure 11(c)) shows the amorphous nature of MCM-41. The HRTEM micrographs of Al_2O_3–MCM-41 also show similar well-ordered hexagonal pores which are shown in Figure 11(d) and 11(e). The amorphous nature of Al_2O_3–MCM-41 is shown in the SAED image (Figure 11(f)). The *in situ* incorporation of Al_2O_3 into the MCM-41 matrix, did not affect the orders of hexagonal pores and amorphous nature of Al_2O_3–MCM-41. The sustainability of amorphous nature in Al_2O_3–MCM-41 is due to the presence of very less amount of crystalline Al_2O_3 in highly amorphous MCM-41 matrix.

The low resolution TEM images of Co@Al_2O_3−MCM-41, Fe@Al_2O_3−MCM-41 and Co- Fe@Al_2O_3−MCM-41 are shown in Figures 12(a) to (c). These pictures confirm that the metal particles in the form of oxide are well dispersed on Al_2O_3−MCM-41 matrix. The metal particles of 4 nm size are seen clearly in the high resolution TEM image of Co-Fe@Al_2O_3−MCM-41 material in Figure 12(d). These particles are in intimate contact with the Al_2O_3−MCM-41 matrix through oxygen atoms. The formation of mono and bimetallic nanoparticles into the mesoporous Al_2O_3−MCM-41 matrix is due to decomposition metal precursor in presence of oleic acid at 120°C. It has been observed that the nucleation and growth of the metal nanoparticles can occur when metal precursor decomposes in the presence of oleic acid at moderate temperatures.[45] The oleic acid has good ability and higher affinity to bind with the surface of the metal oxide nanoparticles. The high binding ability is due to the optimum hydrophilicity and predominant hydrophobicity.[46]

3.5 ^{29}*Si MAS NMR Study*

The ^{29}Si MAS NMR spectra of mesoporous materials such as MCM-41, Al_2O_3−MCM-41 and Co-Fe@Al_2O_3−MCM-41 are shown in Figure 13(a)–(c), respectively. For pure MCM-41, the broad peak around −110, −100 and −91 ppm attributed to Q^4 corresponds to Si $(OSi)_4$, Q^3 corresponds to $(SiO)_3$ Si OH and Q^2 corresponds to $(SiO)_2$ Si $(OH)_2$, respectively. But in Al_2O_3−MCM-41 (Figure 13(b)) the intense peak is observed having peak intensity at −106, −97 and −88 which correspond to Q^4, Q^3 and Q^2, respectively. The downfield shift indicates that the Al atom is coordinated/replaced by the Si atom in the extra-framework of the MCM-41. The ^{29}Si MAS NMR spectrum of Co-Fe@Al_2O_3−MCM-41 is shown in the Figure 13(c). The huge downfield shift of two peaks are observed at −87 (Q^4) and −76 (Q^3) which is due to the coordination of Co and Fe atoms to the Al atom through oxygen or replacement of Si atoms by Co and Fe atoms. This phenomenon proves the formation of mono and bimetallic oxides

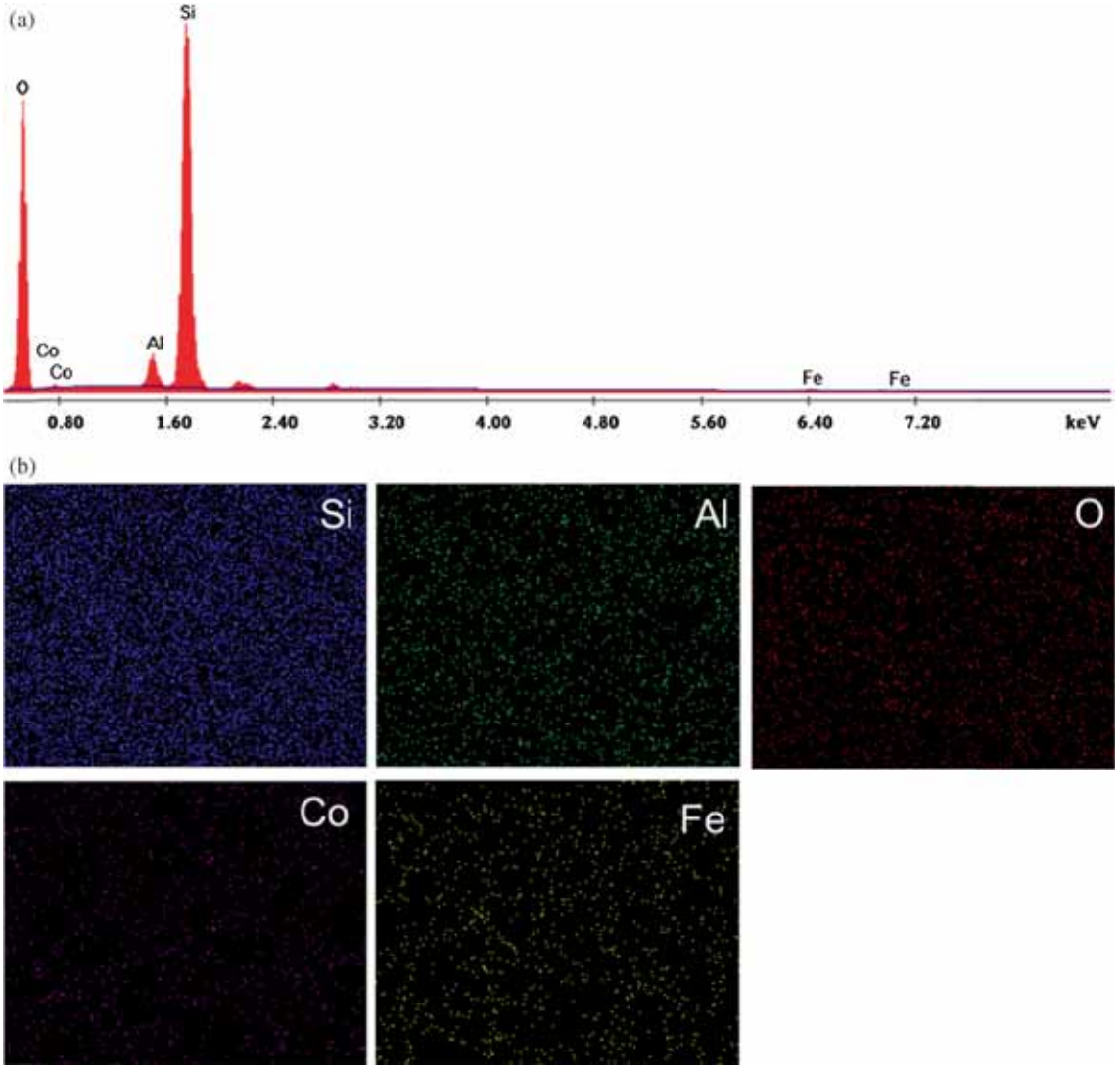

Figure 10. (a) The energy dispersive X-ray (EDX) spectrum of Co-Fe@Al_2O_3−MCM-41; (b) EDX mapping analysis of the Co-Fe@Al_2O_3−MCM-41.

and combines with Al_2O_2 and SiO_2 (MCM-41) within composite.

3.6 *Adsorption studies*

3.6a *Effect of pH*: The pH is the most important factor affecting the adsorption process. When the surfaces of oxide materials containing under-coordinated surface ions come in contact with aqueous environment, their chemical nature strongly depends on the pH of the aqueous phase. They can undergo surface complexation leading to the formation of chemical bonds with water molecules and other adsorbate molecules. The surfaces can undergo protonation and deprotonation in aqueous solutions, affecting the surface charge which is controlled by the pH of the aqueous solution. The surface charge of an oxide material can be positive or negative depending on the pH. If the oxide surface has equal numbers of positively and negatively charged species then the pH at that point is called point of zero charge (pH_{pzc}).[47] Above and below pH_{pzc}, the oxide surface is expected to have net surface charge and promote adsorption processes. We have studied the effect of pH on the adsorption activity of Co-Fe@Al_2O_3−MCM-41. The adsorption of methylene blue on 0.02 g of Co-Fe@Al_2O_3−MCM-41 has been monitored in dark under different pH conditions. The absorbance of the methylene blue solution was measured after 3 h of its exposure to Co-Fe@Al_2O_3−MCM-41 and shown in Figure 14. It was observed that adsorption of methylene blue on Co-Fe@Al_2O_3−MCM-41 is highly favourable at higher pH values. The most efficient adsorption occurred at pH = 10 which is due to the surface charge and generation of surface hydroxyl group in the material. The measured pH_{pzc} value of Co-Fe@Al_2O_3−MCM-41 sample is 3.0 which

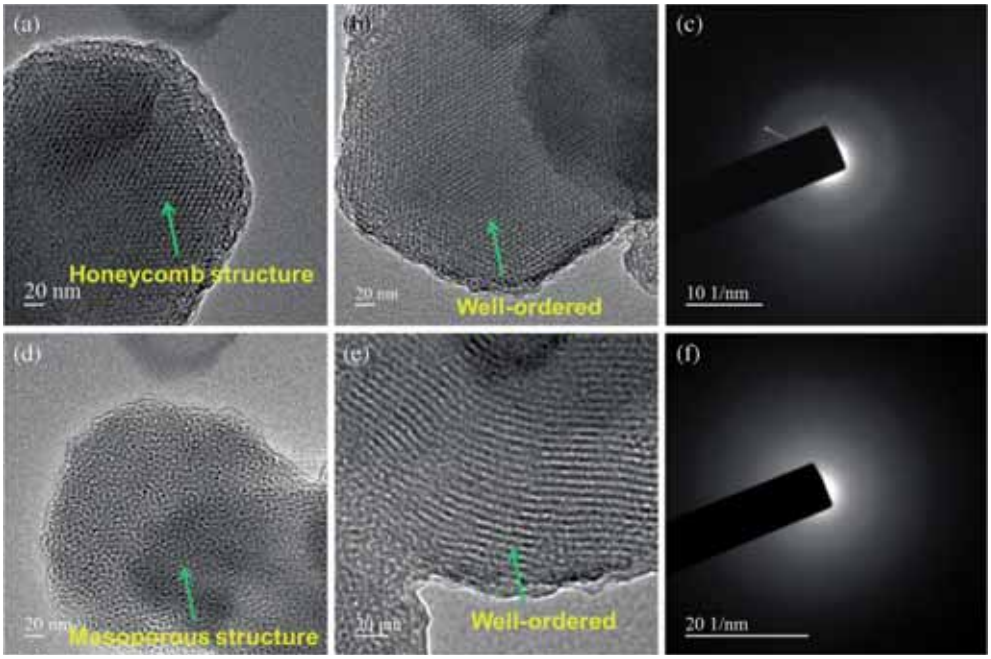

Figure 11. HRTEM images of, (a) honeycomb structure, (b) well-ordered mesoporosity and (c) SAED pattern of MCM-41; HRTEM images of, (d) mesoporous structure, (e) well-ordered nature and (f) SAED pattern of Al_2O_3–MCM-41.

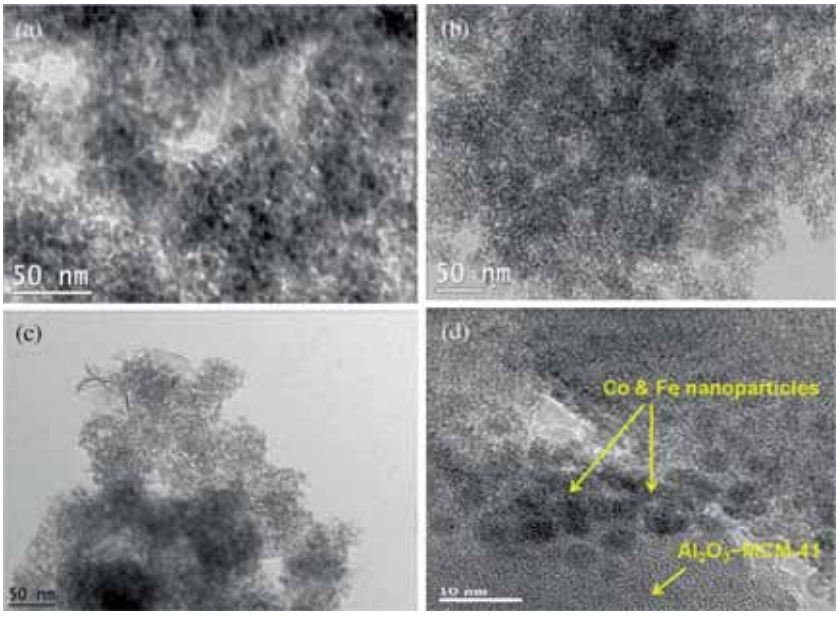

Figure 12. TEM images of, (a) Co@Al_2O_3−MCM-41, (b) Fe@Al_2O_3−MCM-41, (c) Co-Fe@Al_2O_3−MCM-41, (d) HRTEM image of Co-Fe@Al_2O_3−MCM-41 materials.

means the surface is uncharged at pH = 3. Above this pH value, the surface of Co-Fe@Al_2O_3−MCM-41 is expected to be negatively charged and favour methylene blue adsorption through coulombic interactions. The gradual development of negative charges at higher pH is due to the generation of the surface hydroxyl group. In aqueous solution, the surface hydroxyl site of Co-Fe@Al_2O_3−MCM-41 undergoes protonation/deprotonation.[48] So the attraction of cationic MB molecules towards the negative charge surface of Co-Fe@Al_2O_3−MCM-41 will be more at pH = 10. Hence, adsorption of MB is favorable at pH = 10. The methylene blue adsorption decreases gradually from pH = 10 to pH = 2. This is attributed to the presence

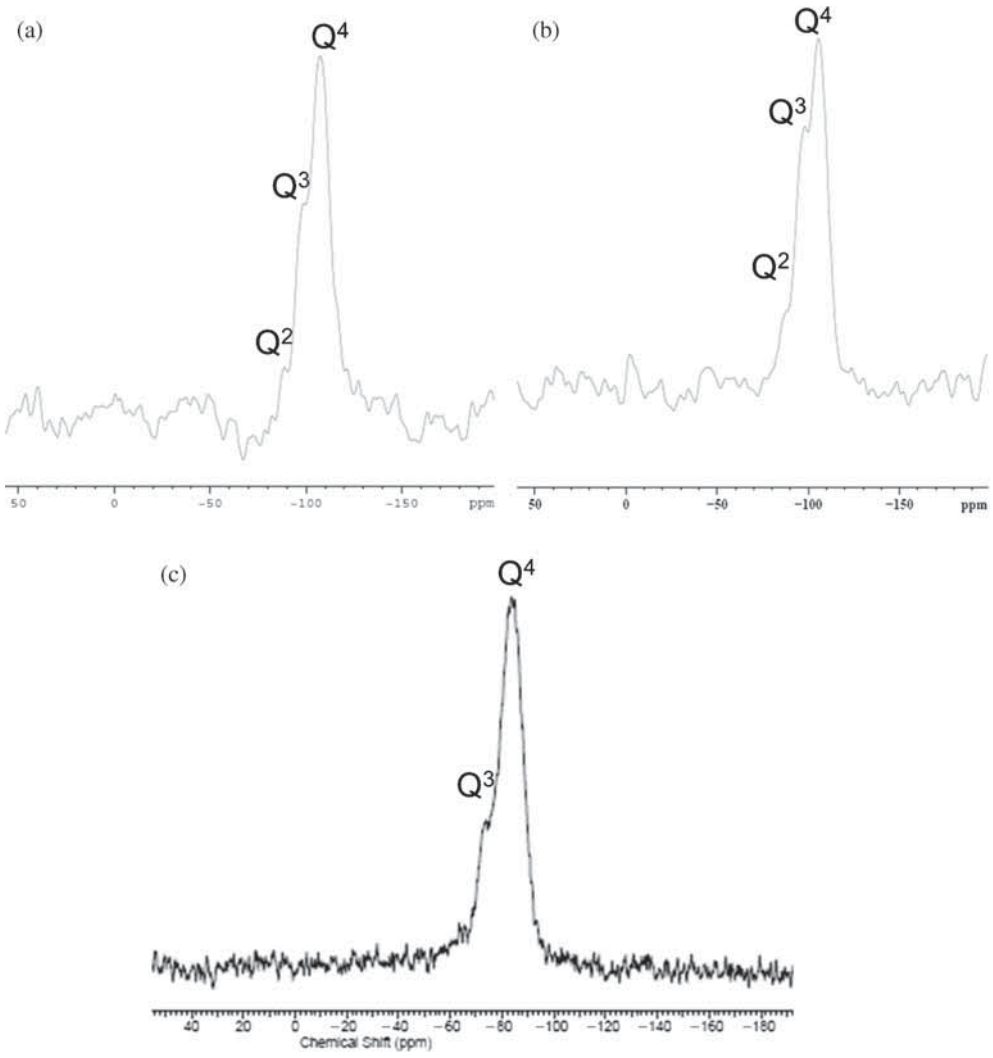

Figure 13. ^{29}Si MAS NMR spectra of, (a) MCM-41, (b) Al_2O_3-MCM-41 and (C) Co-Fe@Al_2O_3- MCM-41.

of excess H^+ ions competing with cationic group of the methylene blue. The percentage of methylene blue adsorbed on the surface of Co-Fe@Al_2O_3-MCM-41 as a function of pH is presented in Supplementary Information (Figure S2). The graph shows that the percentage of methylene blue adsorbed increases with pH of the cationic dye solution which correlates well with negatively charged Co-Fe@Al_2O_3-MCM-41 material. As methylene blue (MB) adsorbed efficiently at pH = 10, hence the MB degradation occurred at optimum condition of pH at 10.

3.6b *Adsorption on different adsorbents*: It has been observed that the maximum amount of MB adsorption occurred at pH = 10. Hence, the adsorption of MB on different adsorbents were carried out at pH = 10. The other optimum parameters such as methylene blue concentration (100 mg/L) and adsorbent amount (0.02 g in 20 mL of MB solution) were taken for this study. The adsorption of methylene blue was carried out in darkness for 3 h by stirring and the supernatant solution was then analysed by UV-Vis spectroscopy. The UV-Vis absorption spectra of the supernatant solutions after methylene blue adsorption by adsorbent are presented in Figure 15. The 100 mg/L pure methylene blue solution shows characteristic absorbance peaks at 664, 615, 292 and 246 nm. The absorbance of the methylene blue solution decreases when treated with different adsorbents under the same experimental conditions. Methylene blue solution (after adsorption) shows the least absorbance with Co-Fe@Al_2O_3-MCM-41 when compared to other adsorbents. Therefore, Co-Fe@Al_2O_3-MCM-41 is a very effective adsorbent which can be attributed its high surface area ($300\,m^2g^{-1}$) and compatible nature of Co-Fe@Al_2O_3-MCM-41 framework. High surface area of Co-Fe@Al_2O_3-MCM-41 material offers more active sites which results increase of MB adsorption. Further, the loading of Al, Fe and Co during synthesis of Co-Fe@Al_2O_3-MCM-41, the Si atoms are coordinated/substituted

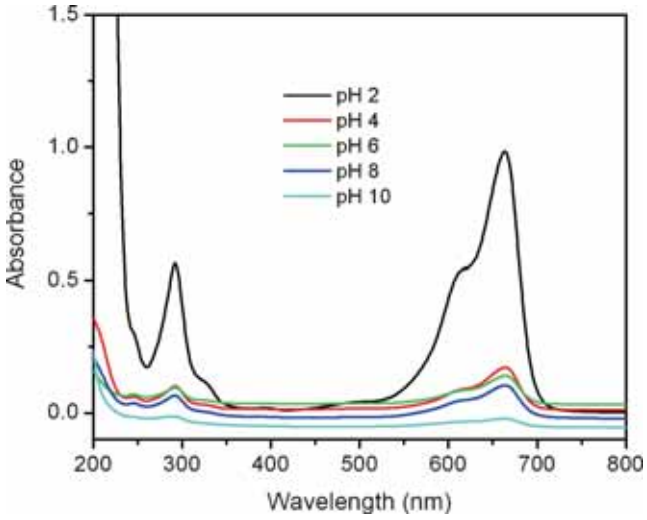

Figure 14. UV-Vis absorption spectra showing the influence of pH on the adsorption of methylene blue on the surface of Co-Fe@Al_2O_3−MCM-41. The pH of the methylene blue solution is varied from 2 to 10. The adsorption process was carried out for 3 h in dark using 100 mg/L methylene blue solution and 0.02 g of Co-Fe@Al_2O_3−MCM-41 material.

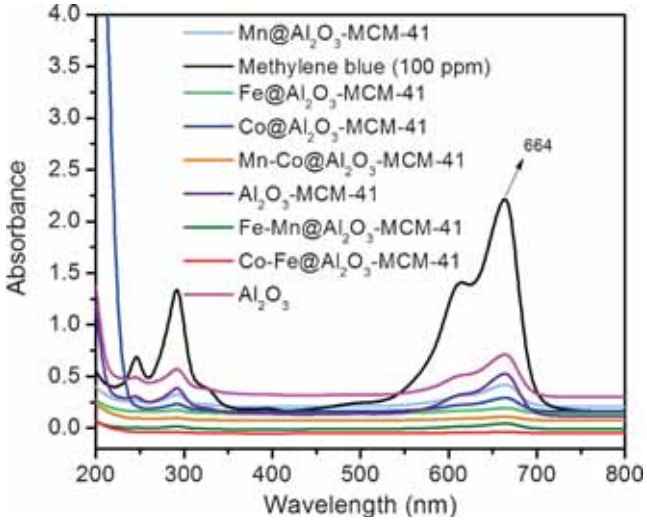

Figure 15. UV-Vis spectra of the solutions recorded after methylene blue adsorption on different adsorbent materials for 3 h in dark at pH=10. The concentration of the methylene blue solution used is 100 mg/L and the amount of adsorbent taken for each experiment is 0.02 g. The decrease in the absorbance of solution is a measure of the removal of methylene blue by adsorption process.

by Al, Fe and Co through oxygen atom. This process helps to generate surface hydroxyl groups. The surface hydroxyl groups of Co-Fe@Al_2O_3−MCM-41 may increase the tendency to form hydrogen bonding with the lone pair electrons of N atom of methylene blue, as shown in Scheme 1. It has been noted that alkaline medium favours high production of surface

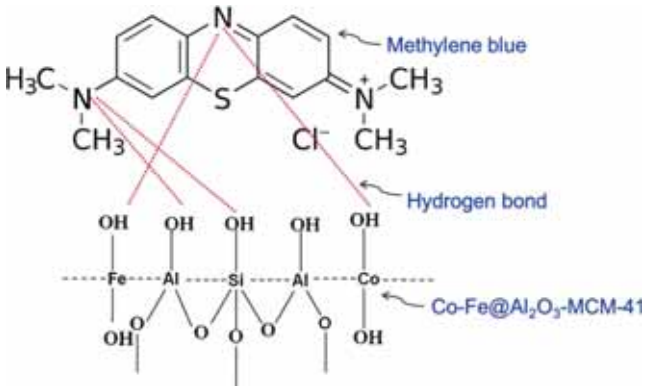

Scheme 1. Hydrogen bond formation between Co-Fe@Al_2O_3–MCM-41 and methylene blue.

hydroxyl group in metal oxide system.[49] It has also been reported that surface hydroxyl group offers a negatively charged surface.[50] Hence, the surface charge of Co-Fe@Al_2O_3−MCM-41 may be more negative which is due to the coordination of more hydroxyl groups with different metal centres such as Co, Fe, Al and Si at pH = 10. The more negative charge surface of Co-Fe@Al_2O_3−MCM-41 could more efficiently adsorb MB as compared to other adsorbents. Moreover, the strong interaction of methylene blue and Co-Fe@Al_2O_3−MCM-41 through hydrogen bonding can also improve the adsorption ability. Furthermore, the molecular volume of methylene blue is 0.4 nm × 0.61 nm × 1.43 nm which is compactable with pore diameter of 2.5 nm and pore volume of 0.9670 $cm^3\ g^{-1}$ in Co-Fe@Al_2O_3−MCM-41. Thus, methylene blue molecule can be accommodated easily into the framework of Co-Fe@Al_2O_3−MCM-41.

Although monometallic@Al_2O_3−MCM-41 materials have high surface area as compared to Co-Fe@Al_2O_3−MCM-41, their adsorption capacity of methylene blue is limited which may be due to the generation of less hydroxyl group and minimal hydrogen bonding ability. Among the bimetallic systems, Co-Fe@Al_2O_3−MCM-41 shows higher ability for methylene blue adsorption compared to other bimetallic systems which can be attributed to the differences in surface areas. The adsorption of methylene blue in bimetallic@Al_2O_3−MCM-41 system follows the order, Co-Fe@Al_2O_3−MCM-41 > Mn-Fe@Al_2O_3−MCM-41 > Co−Mn@Al_2O_3−MCM-41. It is to be noted that the surface area of mesoporous Al_2O_3 is nearly similar the surface areas of mono and bimetallic@Al_2O_3–MCM-41 materials and adsorption capacity is less compared to metal@Al_2O_3–MCM-41 materials. This is due to the absence of more metal onto the Al_2O_3–MCM-41 matrix. The absence of metal onto the Al_2O_3–MCM-41 may not produce more surface hydroxyl group like bimetallic systems. This

may also lead to less hydrogen bonding towards N centre of MB molecule. Hence, presence of metal onto the surface of Al_2O_3–MCM-41 matrix has vital contribution for adsorption of methylene blue.

3.6c *Proof of methylene blue adsorption*: The FTIR spectra of pure methylene blue, methylene blue adsorbed on Co-Fe@Al_2O_3−MCM-41 and neat Co-Fe@Al_2O_3−MCM-41 are shown in the Figures 16(a)–(c), respectively. For pure methylene blue, two peaks appear at 2816, 2720 cm^{-1} which represent the stretching vibration of −CH− aromatic and –CH_3 methyl groups. The spectra ranging from 1591 to 1363 cm^{-1}, are assigned to the aromatic ring structures in methylene blue.[51] The peak at 1170 cm^{-1} is related to the C=C skeleton of the aromatic rings. Figure 16(b) shows strong signature of methylene blue indicating the adsorption of methylene blue on the surface of Co-Fe@Al_2O_3−MCM-41. The IR spectrum of Co-Fe@Al_2O_3−MCM-41 without adsorbed dye molecules is shown Figure 16(c) for comparison. The Figure 16(d) shows the adsorption of methylene blue Co-Fe@Al_2O_3−MCM-41 leading to colourless solution at pH = 10. It should be pointed out that removal of methylene blue can also be promoted by high surface area (300 m^2/g), pore diameter (2.5 nm) and pore volume (0.967 cm^3/g) of Co-Fe@Al_2O_3−MCM-41 material. The molecular dimensions of cationic methylene blue (0.4 nm × 0.61 nm × 1.43 nm) are of the order of pore diameter of Co-Fe@Al_2O_3−MCM-41 and the molecule can be accommodated in the pores very well as shown schematically in Figure 17.

3.6d *Effect of adsorbent dose*: We have further studied the adsorption capacity of Co-Fe@Al_2O_3−MCM-41 material as a function of amount of adsorbent (Figure 18). The amount of methylene blue adsorbed at room temperature has been estimated from UV-Vis absorption spectra of the solutions. The results show that maximum methylene blue adsorption occurs on 0.02 g of Co-Fe@Al_2O_3−MCM-41. Further increase of adsorbent dose does not have much impact on the amount of dye adsorbed.

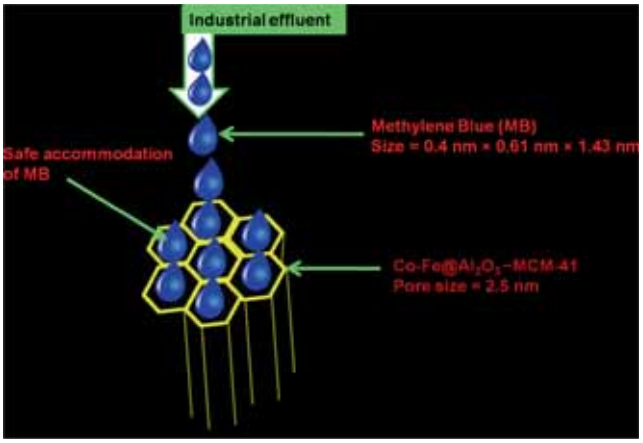

Figure 17. Schematic pathways of methylene blue adsorption on Co-Fe@Al_2O_3−MCM-41.

3.6e *Recovery and recyclability study of adsorbent*: It was difficult to recover quantitatively the adsorbed methylene blue on the surface of Co-Fe@Al_2O_3−MCM-41. It has been reported in the Material Safety Data Sheet (ISO9001:2000 Certified) that the melting point of methylene blue is 100°C. The methylene blue will decompose above 100°C. Methylene blue is removed from the surface of Co-Fe@Al_2O_3−MCM-41 by heating at 180°C for 3 h. The recyclability study was performed to know the stability of the adsorbent

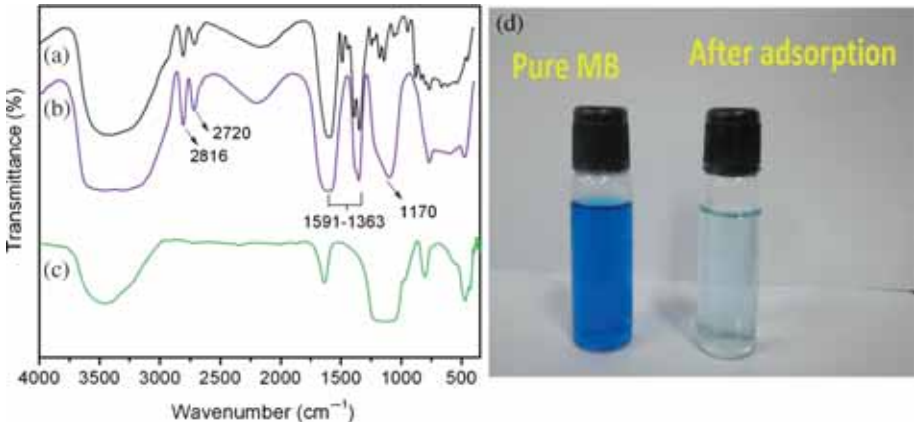

Figure 16. FTIR spectra of (a) pure methylene blue, (b) methylene blue adsorbed on Co-Fe@Al_2O_3−MCM-41 in comparison with (c) Co-Fe@Al_2O_3−MCM-41 material; (d) colour change after adsorption of methylene blue dye (100 mg/L) using 0.02 g of Co-Fe@Al_2O_3−MCM-41 at pH = 10.

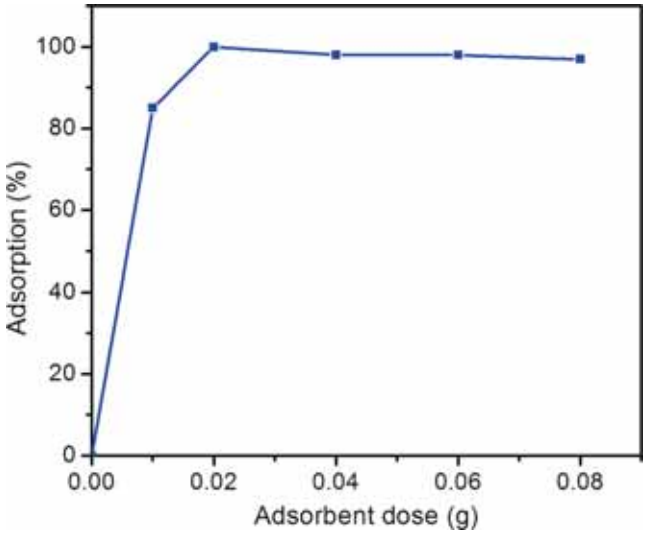

Figure 18. Adsorption capacity of Co-Fe@Al_2O_3−MCM-41 adsorbent as a function of its amount using 20 mL of methylene blue solution (100 mg/L) in each experiment.

Co-Fe@Al_2O_3−MCM-41. The recyclability of Co-Fe @Al_2O_3−MCM-41 was investigated after removal of adsorbed methylene blue on the surface Co-Fe@Al_2O_3−MCM-41 (after heating at 180°C for 3 h). The adsorption process was performed for three runs. The Run 1 was performed on the parent material (Co-Fe@ Al_2O_3−MCM-41) which is showing 100% adsorption shown in the Figure 19. The Co-Fe@Al_2O_3−MCM-41 which was used in Run 1 was recovered by removing the MB at180°C for 3 h. The recovered Co-Fe@Al_2O_3− MCM-41 was used for methylene blue adsorption (Run 2) in similar conditions. Run 3 was performed on the material which was recovered after Run 2. The results (Figure 19) show that there is marginal decrease in the adsorption of MB in recovered Co-Fe@Al_2O_3−MCM-41 adsorbent. This indicates that there may not be change of textural properties like surface area, pore size and pore volume. The textural properties may not change effictively by heating at 180°C for 3 h because the Co-Fe@Al_2O_3−MCM-41 wass stabilied by calcining with 600°C for 6 h at the time of synthesis.

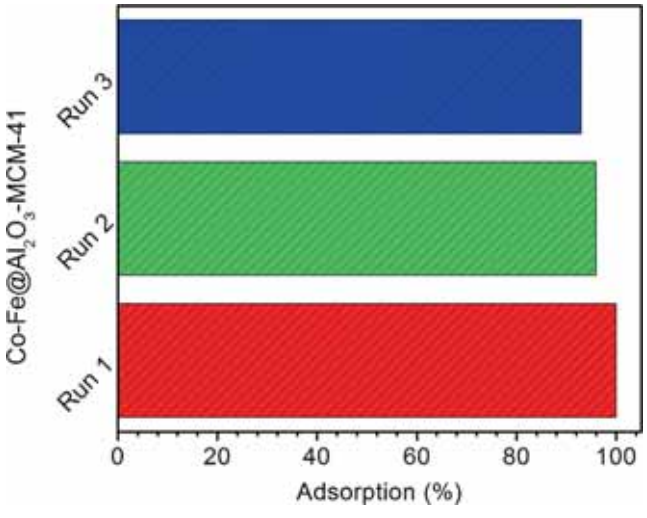

Figure 19. Recycling studies of methylene blue by using Co-Fe@Al_2O_3−MCM-41 as adsorbent. The adsorption process is carried out for 3 h in dark using methylene blue solution (100 mg/L) and 0.02 g of Co-Fe@Al_2O_3−MCM-41. See text for details.

4. Conclusions

In this study, we have highlighted a novel sol-gel-*cum*-hydrothermal method to fabricate mesoporous mono and bimetallic@Al_2O_3−MCM-41 materials. Oleic acid acts as a capping agent for the synthesis of mono and bimetallic oxide nanoparticles onto mesoporous Al_2O_3−MCM-41 material. These materials were found to be very efficient in removing methylene blue from aqueous solutions at pH = 10. Framework mesoporosity, high surface area, appropriate pore diameter and presence of metal nanoparticles are the key factors for high adsorption of methylene blue. The mesoporous Co-Fe@Al_2O_3−MCM-41 is identified as the best adsorbent for methylene blue removal. Quantitatively, 0.02 g of mesoporous bimetallic Co-Fe@Al_2O_3−MCM-41 is sufficient to remove cationic methylene blue dye (100 mg/L) in 20 mL solution.

Supplementary Information (SI)

Additional information pertaining to FTIR spectrum (Figure S1) and methylene blue adsorbed (%) on Co-Fe@Al_2O_3−MCM-41 material (Figure S2) are given in the Supporting Information, which is available at www.ias.ac.in/chemsci.

Acknowledgements

Amaresh Chandra Pradhan thanks IIT Madras for Post-doctoral Fellowship. The instrumental facilities established under the FIST Scheme of SERC division of DST, Ministry of Science and Technology, New Delhi, have been very helpful to carry out this work. Mr. A. Narayanan and Mrs. S. Srividya carried out BET and XRD measurements.

References

1. Tan K B, Vakili M, Horri B A, Poh P E, Abdullah A Z and Salamatinia B 2015 Adsorption of dyes by nanomaterials: Recent developments and adsorption mechanisms *Sep. Purif. Technol.* **150** 229

2. Dias E M and Petit C 2015 Towards the use of metal–organic frameworks for water reuse: A review of the recent advances in the field of organic pollutants removal and degradation and the next steps in the field *J. Mater. Chem. A* **3** 22484
3. Khin M M, Nair A S, Babu V J, Murugan R and Ramakrishna S 2012 A review on nanomaterials for environmental remediation *Energy Environ. Sci.* **5** 8075
4. Yusuf M, Elfghi F M, Zaidi S A, Abdullah E C and Khan M A 2015 Applications of graphene and its derivatives as an adsorbent for heavy metal and dye removal: A systematic and comprehensive overview *RSC Adv.* **5** 50392
5. Bonakala S and Balasubramanian S 2015 Modelling Gas Adsorption in Porous Solids: Roles of Surface Chemistry and Pore Architecture *J. Chem. Sci.* **127** 1687
6. Huang C–H, Chang K–P, Oua H–D, Chiang Y–C and Wanga C–F 2011 Adsorption of cationic dyes onto mesoporous silica *Microporous Mesoporous Mater.* **141** 102
7. Bhaumik A 2002 Mesoporous titanium phosphates and related molecular sieves: Synthesis, characterization and applications *J. Chem. Sci.* **114** 451
8. Sui Z–Y, Cui Y, Zhu J–H and Han B–H 2013 Preparation of Three-Dimensional Graphene Oxide−Polyethylenimine Porous Materials as Dye and Gas Adsorbents *ACS Appl. Mater. Interfaces* **5** 9172
9. He X, Male K B, Nesterenko P N, Brabazon D, Paull B and Luong J H T 2013 Adsorption and Desorption of Methylene Blue on Porous Carbon Monoliths and Nanocrystalline Cellulose *ACS Appl. Mater. Interfaces* **5** 8796
10. Ma J, Yu F, Zhou L, Jin L, Yang M, Luan J, Tang Y, Fan H, Yuan Z and Chen J 2012 Enhanced Adsorptive Removal of Methyl Orange and Methylene Blue from Aqueous Solution by Alkali-Activated Multiwalled Carbon Nanotubes *ACS Appl. Mater. Interfaces* **4** 5749
11. Han B, Zhanga F, Fenga Z, Liub S, Denga S, Wanga Y and Wanga Y 2014 A designed Mn_2O_3/MCM-41 nanoporous composite for methyleneblue and rhodamine B removal with high efficiency *Ceram. Int.* **40** 8093
12. Yagub M T, Sen T K, Afroze S and Ang H M 2014 Dye and its removal from aqueous solution by adsorption: A review *Adv. Colloid Interface Sci.* **209** 172
13. Jyothi D, Deshpande P A, Venugopal B R, Chandrasekaran S and Madras G 2012 Transition metal oxide loaded MCM catalysts for photocatalytic degradation of dyes *J. Chem. Sci.* **124** 385
14. Merka O, Yarovyi V, Bahnemann D W and Wark M 2011 pH-Control of the Photocatalytic Degradation Mechanism of Rhodamine B over $Pb_3Nb_4O_{13}$ *J. Phys. Chem. C* **115** 8014
15. Zhou X, Yang H, Wang C, Mao X, Wang Y, Yang Y and Liu G 2010 Visible Light Induced Photocatalytic Degradation of Rhodamine B on One-Dimensional Iron Oxide Particles *J. Phys. Chem. C* **114** 17051
16. Guo B, Shen H, Shu K, Zeng Y and Ning W 2009 The study of the relationship between pore structure and photocatalysis of mesoporous TiO_2 *J. Chem. Sci.* **121** 317
17. Uddin M T, Nicolas Y, Olivier C, Toupance T, Muiller M M, Kleebe H J, Rachut K, Ziegler J, Klein A and Jaegermann W 2013 Preparation of RuO_2/TiO_2 Mesoporous Heterostructures and Rationalization of Their Enhanced Photocatalytic Properties by Band Alignment Investigations *J. Phys. Chem. C* **117** 22098
18. Jain A, Lodha S, Punjabi P B, Sharma V K and Ameta S C 2009 A study of catalytic behaviour of aromatic additives on the photo–Fenton degradation of phenol red *J. Chem. Sci.* **121** 1027
19. Tian S, Zhang J, Chen J., Kong L, Lu J, Ding F and Xiong Y 2013 $Fe_2(MoO4)_3$ as an Effective Photo-Fenton-like Catalyst for the Degradation of Anionic and Cationic Dyes in a Wide pH Range *Ind. Eng. Chem. Res.* **52** 13333
20. Parida K M and Pradhan A C 2010 Fe/meso-Al_2O_3: An Efficient Photo-Fenton Catalyst for the Adsorptive Degradation of Phenol *Ind. Eng. Chem. Res.* **49** 8310
21. Pradhan A C and Parida K M 2012 Facile synthesis of mesoporous composite Fe/Al_2O_3–MCM-41: An efficient adsorbent/catalyst for swift removal of methylene blue and mixed dyes *J. Mater. Chem.* **22** 7567
22. Hsu C A, Wen T N, Su Y C, Jiang Z B, Chen C W and Shyur L F 2012 Biological Degradation of Anthroquinone and Azo Dyes by a Novel Laccase from Lentinus sp *Environ. Sci. Technol.* **46** 5109
23. Swathi R S and Sebastian K L 2012 Excitation energy transfer from dye molecules to doped graphene *J. Chem. Sci.* **124** 233
24. Bi H, Xie X Yin K, Zhou Y, Wan S, He L, Xu F, Banhart F, Sun L and Ruoff R S 2012 Spongy Graphene as a Highly Efficient and Recyclable Sorbent for Oils and Organic Solvents *Adv Funct. Mater.* **22** 4421
25. Ramesha G K, Kumara A V, Muralidhara H B and Sampath S 2011 Graphene and graphene oxide as effective adsorbents toward anionic and cationic dyes *J. Colloid Interface Sci.* **361** 270
26. Chowdhury S and Balasubramanian R 2014 Recent advances in the use of graphene-family nanoadsorbents for removal of toxic pollutants from wastewater *Adv. Colloid Interface Sci.* **204** 35
27. Jiang S -D, Tang G, Ma Y F, Hu Y and Song L 2015 Synthesis of nitrogen-doped graphene−ZnS quantum dots composites with highly efficient visible light photodegradation *Mater. Chem. Phys.* **151** 34
28. Lam K F, Yeung K L and Mckay G 2007 Selective mesoporous adsorbents for $Cr_2O_7^{2-}$ and Cu^{2+} separation *Microporous Mesoporous Mater.* **100** 191
29. Chen X, Lam K F, Zhang Q, Pan B, Arruebo M and Yeung K L 2009 Synthesis of Highly Selective Magnetic Mesoporous Adsorbent *J. Phys. Chem. C* **113** 9804
30. Pelekani C and Snoeyink V L 2000 Competitive adsorption between atrazine and methylene blue on activated carbon: The importance of pore size distribution *Carbon* **38** 1423
31. Eftekhari S, Habibi-Yangjeh A and Sohrabnezhad S 2010 Application of AlMCM-41 for competitive adsorption of methylene blue and Rhodamine B: Thermodynamic and kinetic studies *J. Hazard. Mater.* **178** 349
32. Nguyen T B Hwang M J and Ryu K–S 2012 High adsorption capacity of V-doped TiO_2 for decolorization of methylene blue *Appl. Surf. Sci.* **258** 7299
33. Gutierrez-Alejandre A, Larrubia M A, Ramirez J and Busca G 2006 FT-IR evidence of the interaction of benzothiophene with the hydroxyl groups of H-MFI and H-MOR zeolites *Vib. Spectrosc.* **41** 42

34. Parida K M, Pradhan A C, Das J and Sahu N 2009 Synthesis and characterization of nano-sized porous gamma-alumina by control precipitation method *Mater. Chem. Phys.* **113** 244
35. Guthrie C P and Reardon E J 2008 Metastability of MCM-41 and Al-MCM-41 *J. Phys. Chem. A* **112** 3386
36. Konovalova T A, Gao Y, Schad R and Kispert L D 2001 Photooxidation of Carotenoids in Mesoporous MCM-41, Ni-MCM-41 and Al-MCM-41 Molecular Sieves *J. Phys. Chem. B* **105** 7459
37. Li S, Xu Q, Chen J and Guo Y 2008 Study and Characterization of Al-MCM-41 Prepared with the Assistance of Supercritical CO_2 *Ind. Eng. Chem. Res.* **47** 8211
38. Brunaure S, Deming L S, Deming W E and Teller E 1940 On a Theory of the van der Waals Adsorption of Gases *J. Am. Chem. Soc.* **62** 723
39. Tanev P T and Pinnavaia T J 1996 Mesoporous Silica Molecular Sieves Prepared by Ionic and Neutral Surfactant Templating: A Comparison of Physical Properties *Chem. Mater.* **8** 2068
40. Goyne K W, Zimmerman A R, Newalkar B L, Komarneni S, Brantley S L and Chorover J 2002 Surface Charge of Variable Porosity $Al2O_3$(s) and SiO_2(s) Adsorbents *J. Porous Mater.* **9** 243
41. Selvaraj M and Pandurangan A 2004 Comparison of Mesoporous Zn-Al-MCM-41 and Al-MCM-41Molecular Sieves in the Production of *p*-Cymene by Isopropylation of Toluene *Ind. Eng. Chem. Res.* **43** 2399
42. Greenwood N N and Earnshaw A 1998 In *Chemistry of the Elements* (UK: Reed Educational and Professional Publishing) p.1341
43. Selvaraj M, Sinha P K, Lee K, Ahn I, Pandurangan A and Lee T G 2005 Synthesis and characterization of Mn–MCM-41 and Zr–Mn-MCM-41 *Microporous Mesoporous Mater.* **78** 139
44. Atchudan R, Pandurangan A and Joo J 2013 Synthesis of multilayer graphene balls on mesoporous Co-MCM-41 molecular sieves by chemical vapour deposition method *Microporous Mesoporous Mater.* **175** 161
45. Moya C, Batlle X and Labarta A 2015 The effect of oleic acid on the synthesis of $Fe_{3-x}O4$ nanoparticles over a wide size range *Phys. Chem. Chem. Phys.* **17** 27373
46. Arulmozhi K T and Mythili N 2013 Studies on the chemical synthesis and characterization of lead oxide nanoparticles with different organic capping agents *AIP Adv.* **122122** 1
47. Churchill H, Teng H and Hazen R M 2004 Correlation of pH-dependent surface interaction forces to amino acid adsorption: Implications for the origin of life *Am. Mineral.* **89** 1048
48. Hu Q H, Qiao S Z, Haghseresht F, Wilson M A and Lu G Q 2006 Adsorption Study for Removal of Basic Red Dye Using Bentonite *Ind. Eng. Chem. Res.* **45** 733
49. Sengupta A K 2016 In *Ion Exchange and Solvent Extraction*: *A Series of Advances* (Boca Raton: CRC Press) vol. 22 p. 178
50. Papirer E 2000 In *Adsorption on Silica Surfaces* (New York: CRC Press) vol. 90 p. 442
51. Lau Y–Y, Wong Y–S, Teng T–T, Morad N M and Rafatullah S–A O 2015 Degradation of cationic and anionic dyes in coagulation–flocculation process using bi-functionalized silica hybrid with aluminum-ferric as auxiliary agent *RSC Adv.* **5** 34206